Nanoscale Advances

ROYAL SOCIETY OF CHEMISTRY

PAPER

View Article Online
View Journal | View Issue

Cite this: *Nanoscale Adv.*, 2023, **5**, 3348

Strong quenching of dye fluorescence in monomeric perylene orange/TMDC hybrid structures†

Tim Völzer, [ab] Alina Schubert, [ab] Erik von der Oelsnitz,[ab] Julian Schröer, [ab] Ingo Barke,[ab] Rico Schwartz,[a] Kenji Watanabe, [c] Takashi Taniguchi,[d] Sylvia Speller,[ab] Tobias Korn [ab] and Stefan Lochbrunner [ab]*

Hybrid structures with an interface between two different materials with properly aligned energy levels facilitate photo-induced charge separation to be exploited in optoelectronic applications. Particularly, the combination of 2D transition metal dichalcogenides (TMDCs) and dye molecules offers strong light–matter interaction, tailorable band level alignments, and high fluorescence quantum yields. In this work, we aim at the charge or energy transfer-related quenching of the fluorescence of the dye perylene orange (PO) when isolated molecules are brought onto monolayer TMDCs *via* thermal vapor deposition. Here, micro-photoluminescence spectroscopy revealed a strong intensity drop of the PO fluorescence. For the TMDC emission, in contrast, we observed a relative growth of the trion *versus* exciton contribution. In addition, fluorescence imaging lifetime microscopy quantified the intensity quenching to a factor of about 10^3 and demonstrated a drastic lifetime reduction from 3 ns to values much shorter than the 100 ps width of the instrument response function. From the ratio of the intensity quenching that is attributed to hole or energy transfer from dye to semiconductor, we deduce a time constant of several picoseconds at most, pointing to an efficient charge separation suitable for optoelectronic devices.

Received 25th April 2023
Accepted 22nd May 2023

DOI: 10.1039/d3na00276d

rsc.li/nanoscale-advances

1. Introduction

In the past decade, transition metal dichalcogenides (TMDCs) have emerged as 2D semiconductors. The key features of these materials are the transition from indirect to direct semiconductors, which is accompanied by the emergence of their photoluminescence,[1,2] as well as a drastic rise of the exciton binding energy when thinned down from bulk to a monolayer (1L).[3] This shifts the recombination dynamics from the regime of Auger scattering of free carriers to being governed by the diffusion of excitons.[4,5] In combination with the strong light–matter interaction, these monolayer properties promise potential applications in photonics and optoelectronics ranging from LEDs to photodetectors.[6] In the latter case, charge separation and transfer following optical excitation can be facilitated by the fabrication of heterostructures, where 1L-TMDCs are combined with one another,[7,8] other 2D semiconductors,[9] graphene,[10] or hybrid structures with 0D objects such as small molecules or quantum dots, 1D nanostructures, as well as 3D bulk materials.[11,12] As an already established research field, TMDC heterostructures represent the first choice among the above named. Here, ultrafast charge transfer times of 50 fs and less have been found.[13,14] Yet, these heterostructures remain limited regarding their performance and costs.[11]

Beyond such heterostructures, the combination of 2D semiconductors with dye molecules brings several benefits on its own, which touch different aspects of the systems. First, on the fundamental side, hybrid structures allow the combination of two contrary regimes of exciton mobility, namely the discrete Förster transfer between essentially 0D molecules[15,16] as opposed to the continuous exciton diffusion in the 2D TMDCs.[4,5] Second, from a preparational point of view, many methods for molecule deposition on surfaces can be scaled, offering the opportunity of preparing large-area hybrid structures, starting from full-coverage chemical vapor deposition (CVD-)grown monolayers.[17,18] Third, the band levels of molecules such as perylene diimides (PDIs) can easily be tailored by exchanging their organic substituents,[19] while their optical spectra exhibit characteristic shapes that significantly change

[a]*Institute of Physics, University of Rostock, Albert-Einstein-Str. 23, 18059 Rostock, Germany. E-mail: stefan.lochbrunner@uni-rostock.de*

[b]*Department "Life, Light and Matter", University of Rostock, Albert-Einstein-Str. 25, 18059 Rostock, Germany*

[c]*Research Center for Electronic and Optical Materials, National Institute for Materials Science, 1-1 Namiki, Tsukuba 305-0044, Japan*

[d]*Research Center for Materials Nanoarchitectonics, National Institute for Materials Science, 1-1 Namiki, Tsukuba 305-0044, Japan*

† Electronic supplementary information (ESI) available: Parametrization of preparation techniques, photodegradation of dye molecules, AFM scans, PL results at 10 K, additional FLIM results for the hBN, MoS_2, $MoSe_2$, and WS_2 samples and without the use of the band pass filter. See DOI: https://doi.org/10.1039/d3na00276d

upon aggregation[20] or charge transfer.[21] Finally, in view of spectroscopic investigations, the near-unity fluorescence quantum yield of these dyes ensures strong signals,[19] in contrast to typical values below 1% for pristine 1L-TMDCs.[1,22]

Several studies on hybrid molecule/1L-TMDC structures have been conducted with their focus lying on changes of the photoluminescence from the TMDC monolayer.[23–26] To that end, comparably thick dye layers of several 10 nm have been deposited. In this case, the molecules function as an essentially infinite charge trap, *i.e.* draining excited electrons or holes from the absorbing TMDC layer on a timescale of picoseconds.[27–30]

In the inverse situation, where molecular layers (of several nm thickness) on a 2D material are excited, the charge transfer takes place towards the TMDC and proceeds significantly faster, with reported upper limits for the time constants of a few 100 fs down to 40 fs. The charge transfer is typically followed by thermal relaxation of the hot charge carriers or interlayer excitons, even spin flips and the formation of triplet excitons may occur.[29–32]

While these studies mostly focus on nanometer films of electron-donating metal phtalocyanine molecules[30–33] on MoS_2, investigations with purely organic dyes such as the electron-accepting PDIs were conducted in wet media.[21,34] In this work, however, we create hybrid structures by vapor depositing monomeric dye molecules of the PDI *N*,*N*′-bis(2,6-diisopropylphenyl)-3,4,9,10-perylenetetracarboxylic diimide, commonly referred to as perylene orange (PO). In contrast to previous studies, we chose a molecular coverage well below a monolayer, creating essentially 0D regimes as opposed to 2D continuous or even 3D bulk-like dye films. As the inorganic counterpart in the hybrid structures and deposition target, we prepared mechanically exfoliated monolayer flakes of the four most common TMDCs (MX_2 with M = Mo, W and X = S, Se) as well as multilayer hexagonal boron nitride (hBN) as a reference. Fig. 1 shows their relevant energy levels, that is the valence band (VB) maximum and conduction band (CB) minimum for the 2D materials and the highest occupied and lowest unoccupied molecular orbital (HOMO and LUMO, respectively) of the dye. When a photon is absorbed by the PO (TMDC), an electron from the HOMO (VB) will be raised to the LUMO (CB), leaving a hole in the HOMO (VB) with whom it forms an exciton. As the hBN band gap completely comprises the relevant energy levels of PO, neither charge nor energy transfer is expected from the dye into the hBN. For each of the PO/TMDC hybrids, in contrast, both processes are possible, offering a rapid nonradiative decay channel. Consequently, we expect the fluorescence lifetime to shorten drastically and the intensity to decrease strongly, as the molecular exciton will less likely recombine radiatively. Thus, we investigate the hybrids *via* spectrally, spatially and temporally resolved emission spectroscopy.

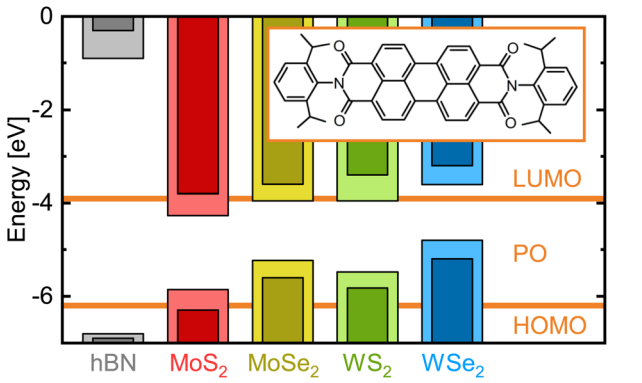

Fig. 1 Electronic energy levels of various 2D materials *versus* perylene orange. The vacuum level is set to zero. The horizontal lines show the HOMO and LUMO energies of the isolated dye molecule, whose molecular structure is depicted in the inset.[35] Pale and dark bars indicate the value range for VBM and CBM energies extracted from various publications reporting on density functional theory calculations (hBN;[36] MoS_2;[23,27,37–39] $MoSe_2$;[23,38–40] WS_2;[28,37–39,41] WSe_2 (ref. 23, 38 and 39)). In these calculations, excitonic effects were not considered. While the hBN band levels lie far from the molecular orbitals, for each TMDC, at least one of the band extrema falls into the HOMO–LUMO-gap of PO.

2. Experimental

Hybrid structures were prepared by thermal vapor deposition (TVD) of monomer PO films onto mechanically exfoliated 2D flakes transferred to Si/SiO_2 wafers.[42] PO powder (Exciton, Exalite 578) is heated to temperatures from 430 K to 450 K and evaporated in vacuum ($\leq 1 \times 10^{-2}$ mbar) in order for the molecules to condense onto the target substrate kept at about room temperature. The total process duration amounted to 40 min, including roughly 15 min of heating up the powder reservoir from room to the evaporation temperature. The specific evaporation temperature was adjusted to the target coverage by coating glass slides as references in advance. Here, we aimed at a coverage of about 2.4×10^{-2} nm^{-2}, corresponding to roughly $\frac{1}{30}$ of a monolayer and ensuring the monomeric behavior of the deposited molecules (see ESI, Sections 1.1 and 1.2†). As an alternative coating technique, stamping was also tested in Section 1.3 of the ESI.† This offers a low-threshold method similar to the deterministic transfer of 2D materials. However, it yields more inhomogeneous molecular films.

For micro-photoluminescence (μ-PL) spectroscopy, a 532 nm (RLTMGL-532-100-3, Roithner) or 633 nm (OBIS 633LXSF, Coherent) continuous wave laser is focused onto the sample. The emitted radiation is collected by a microscope objective, filtered from the scattered excitation light using a long-pass plus a spatial filter with a 50 μm pinhole, and analyzed by a grating spectrometer (Acton 2300i). In our experiments, the excitation power was about 4.5 μW for the green and 9 μW for the red laser, with a focus diameter of about 1.0 μm to 1.5 μm. The sample was scanned beneath the fixed optical beam path to obtain a 2D raster of the relevant area, with one spectrum acquired at each position within 1 s. To prevent photooxidation of the dye molecules,[43] the samples were kept in vacuum during the experiment. An investigation of photodegradation under ambient conditions is presented in the ESI, Section 2.† If not mentioned otherwise, all measurements were conducted at room temperature and employing the green laser. The cooling

for low-temperature scans was provided by liquid nitrogen for 80 K and by liquid helium for 10 K.

Fluorescence lifetime imaging microscopy (FLIM) measurements were performed using the MicroTime 200 system by PicoQuant. In these experiments, the sample is excited by 442 nm pulses with an energy of 0.3 pJ at a repetition rate of 40 MHz (equivalent to 12.5 μW), focused down to a diameter of 0.9 μm. The emitted light is detected *via* time-correlated single photon counting, yielding a high sensitivity as well as a time resolution of about 100 ps. Analogously to the μ-PL spectroscopy, the sample area is scanned to obtain a 2D map, with a dwell time of 50 ms per pixel. This short exposure time is crucial to minimize the photodegradation of the dye in those measurements, as they have to be conducted under ambient conditions. Another difference of this setup compared to the μ-PL spectroscopy lies in the lack of spectral resolution. Consequently, we are not able to separate the PO fluorescence from the contributions of the monolayer photoluminescence (see ESI, Section 4.2†). To solve this problem, we placed a 50 nm band pass filter with a central wavelength of 525 nm in the probe beam right in front of the detector, in addition to the standard filters for blocking the excitation light. We tested the filter performance using 1L-WS_2, which – among the four investigated TMDCs – has the strongest PL (in that particular setup) that is also the closest to the filter transmission range. Here, we demonstrated an intensity suppression of the PL by a factor of about 10^4. As a positive side-effect, the selected spectral range roughly matches the 0–0-peak of the dye fluorescence. When comparing this to the spectra of any agglomerated molecular species (see ESI, Sections 1 and 3†), we find that those contributions are essentially excluded from the signal. Accordingly, the measurements with the band pass filter are mostly sensitive to the monomer PO. The instrument response function (IRF) was determined as the detected time trace of the back-reflected excitation light. It was measured using a blank wafer sample and omitting both filters. Here, we extracted an IRF duration of about 150 ps (FWHM) with an asymmetry in terms of a prolonged tail at positive times.

3. Spectral emission landscape of hybrid structures

To characterize the deposited molecular films and their interaction with the substrate or the underlying flakes, we conducted optical experiments on TVD-fabricated 1L-TMDC/PO and hBN/PO hybrid structures. First, μ-PL spectroscopy was performed to elaborate any spectral changes that would indicate a coupling between the 2D material and the dye molecules or even within the molecular layer.

Fig. 2(a) and (d) show two investigated hybrid structures of PO on hBN and WSe_2, respectively, with the resulting μ-PL spectra being depicted in (c) for PO on the wafer substrate, on hBN, and on 1L-WSe_2. Despite the use of a long-pass filter, a sharp peak from the excitation light remains around 2.33 eV. Although the long-pass filter weakens the 0–0 band of the molecular fluorescence band, PO contributes the characteristic multi-peak Franck–Condon structure of its emission.[19] This indicates dye monomers as the dominant species (Spectral signatures of other species are discussed in the ESI, Sections 1.1 and 3†). Additionally, the monolayer WSe_2 flake features a strong, sharp, and distinct photoluminescence peak at around 1.65 eV. This allows a spectral separation of the two emission bands, facilitating a separate mapping of the integrated dye fluorescence (1.8 eV to 2.325 eV) and 1L-PL intensity (1.6 eV to 1.7 eV), as depicted in Fig. 2(b), (e) and (f), respectively. The so-obtained integrated intensity maps reproduce the crystal topography, as can be seen comparing Fig. 2(a) and (d) with Fig. 2(b) and (e). When regarding the spectral range of the semiconductor PL (Fig. 2(f)), the monolayer regions clearly stand out of their dark surroundings, as expected by the strong luminescence enhancement due to the transition from direct to indirect band gaps in TMDC monolayers compared to thicker flakes.[1,2] The dye fluorescence, on the other hand, appears weaker on the hBN flakes compared to the wafer substrate and vanishes almost completely in the PO/WSe_2 hybrid, as evident in the PL spectra as well. For an ideal PO/hBN hybrid structure, we would not expect any modulation or reduction of the fluorescence intensity, given the band level alignment. In reality, the moderate intensity drop on the hBN can be caused by adsorbed species acting as charge traps.[44] Alternatively, it could be that during TVD, evaporated molecules less likely deposit on hBN compared to the SiO_2 surface of the wafer, resulting in a lower PO coverage and correspondingly lower signal. Nevertheless, sufficiently many PO molecules reside on top of the flake, since the dye fluorescence is clearly detected from the hBN area. Due to the similarity of the hBN and TMDC surfaces, we assume a similar molecule coverage on the WSe_2 flake. We conclude that in this case, the PO emission is unambiguously quenched as a consequence of charge or energy transfer into the TMDC.

With the suppression of the dye fluorescence below the experimental sensitivity, we turn to investigate the WSe_2 PL counterpart in more detail to track changes introduced by the deposited molecules. Under this scope, low-temperature measurements offer the distinction of different emission features like neutral excitons and charged ones, *i.e.* trions,[45] whose balance reacts to changes in doping or defect availability.[46] PL spectra acquired at liquid nitrogen temperature show a clear separation of the exciton (X^0) and negative trion (X^-, identified *via* measurements at 10 K, see ESI Section 4.1†) emission bands (Fig. 3). Upon deposition of PO, the latter grows relatively to the former. On first sight, this appears as a sign for charge transfer.[33] In our case, however, this interpretation would contradict the band alignment of PO and 1L-WSe_2, as depicted in Fig. 1, since electrons would have to migrate energetically uphill towards the WSe_2 CB or holes downhill into the PO HOMO. In other words, the observed change in the trion emission is of opposite sign as the charge transfer expected from the band levels. Furthermore, the spectral shape is independent of the excitation wavelength and thus unaffected by whether the molecules are excited or not. Ergo, the major effect originates already from the presence of molecules in their electronic ground state. A possible explanation for the enhanced trion PL could arise from changes in the nonradiative recombination

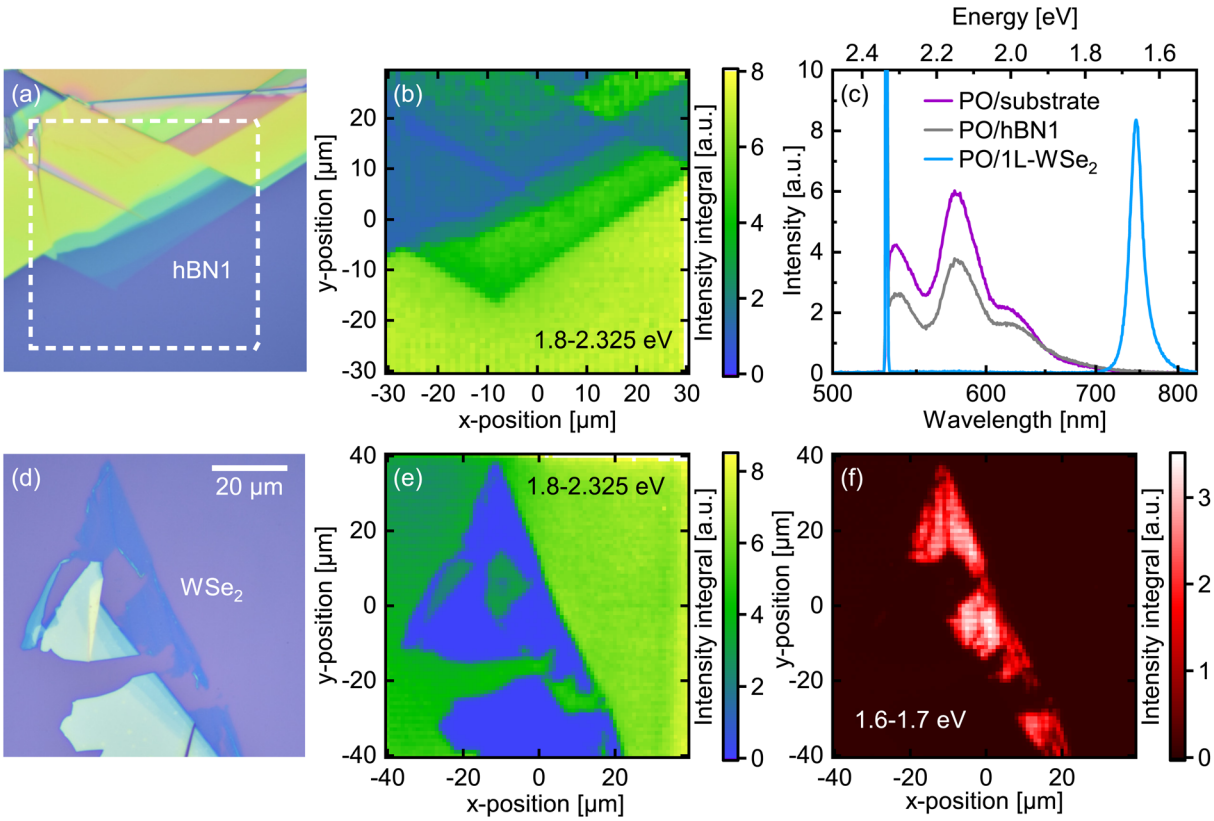

Fig. 2 µ-PL spectroscopy after excitation of TVD-coated hBN and WSe_2 at 532 nm. (a and d) Micrographs of the sample flakes and their environment. The dashed square in (a) marks the area depicted in (b), while (d)–(f) show identical regions. (b and e) Integrated PO fluorescence intensity maps. The intensity appears slightly lower on the thin hBN and almost zero on the WSe_2 flake compared to the surrounding substrate. (c) PL spectra of PO on different 2D crystals *vs.* substrate reference. The sharp peak at 2.33 eV is assigned to stray light from the excitation, the three-peak structure matches the PO emission, and the single low-energy contribution corresponds to the monolayer WSe_2 PL. (f) Integrated 1L-WSe_2 PL intensity map. The monolayer part stands out brightly from the surrounding thicker crystals and the substrate.

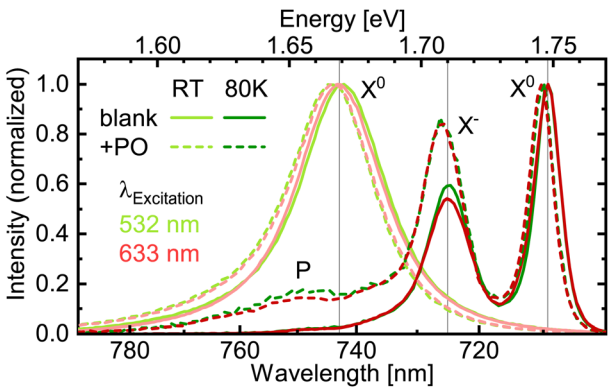

Fig. 3 Normalized PL spectra of blank WSe_2 (solid lines) and PO/WSe_2 hybrid structure (dashed lines) at room temperature and 80 K (bright and dark colors, respectively) after excitation at 532 nm (green) and 633 nm (red). The latter are pairwise essentially identical. At low temperature, the 1L-PL blue-shifts and splits up spectrally into exciton (X^0) and negative trion (X^-) emission. Upon deposition of the dye molecules, the trion contribution grows relative to the excitonic one. Additionally, a weak signal appears at 750 nm (marked as P).

channels in 1L-WSe_2. Deposited molecules could screen defects, thereby reducing the rate for trapping at those sites[24,47] that takes place within several 10 ps at room temperature.[4] This would largely benefit the trionic emission that occurs on similar time scales while the comparatively short-living excitons remain relatively unaffected.[48,49] Consequently, the peak ratio might evolve in favor of the negative trions without an actual change of the doping. In principle, this effect could even conceal a minor charge transfer in the (expected) opposite direction. As an alternative explanation, the deposition of PO molecules could eliminate other adsorbates that initially suppressed the formation of or the emission from negative trions. Either way, the dye molecules apparently do not drain enough electrons from or – if excited – inject enough holes into the 1L-WSe_2 to significantly alter the charge balance there. This appears reasonable, given the low dye coverage of 2.4×10^{12} cm^{-2}, *i.e.* one molecule per roughly 40 nm^2 (see ESI, Section 1.2†) compared to the areal size of the 1L-WSe_2 unit cell of 0.1 nm^2 ($\equiv 10^{15}$ cm^{-2}).[39] Hence, in this coverage regime, molecular functionalization does not affect the doping level of 2D semiconductors significantly. Indeed, studies that observed a pronounced charge transfer-related change of the exciton–trion balance employed much thicker molecular layers of several nm.[33] In addition to the excitonic and trionic peak, we observe a weak emission band (P) around 750 nm that emerges in the hybrid structure at low temperatures. While a detailed investigation of this feature exceeds the scope of this work, several possible physical origins are conceivable. First, the

emission could stem from the triplet state T_1 of PO. For perylene derivatives, these states usually lie energetically low, frequently down to half of the singlet S_1 energy.[50] However, this phosphorescence would be expected to exhibit a spectral width comparable to the fluorescence peaks, which does not hold for the P contribution.[51] Second, excitons and trions could combine to form (charged) biexcitons (see ESI Section 4.1†) or bind to defects, creating localized, yet luminescent excitons.[52,53] This process could be enabled by the deposited dye molecules either *via* the modified Fermi level or the screening of defects. Finally, the emission peak could be a sign of interlayer exciton formation, where the electron resides in the PO layer and the hole in the WSe_2.[28,54,55]

Summing up the μ-PL measurements, we found a strong indication for fluorescence intensity quenching as well as a relatively enhanced trion PL when combining PO with WSe_2 in a hybrid structure. Yet, we cannot distinguish unambiguously between charge and energy transfer as the dominant contribution to the fluorescence quenching. Nevertheless, as charge transfer is generally observed in type II band alignments,[27–33] we favor this interpretation. Even if energy transfer would outcompete hole transfer from the molecular into the semiconductor layer, a consecutive back-transfer of electrons is expected in PO/WSe_2 hybrids, resulting in charge separation after all.[30] Regardless of the specific mechanism responsible for the quenching, any fast nonradiative decay channel does not only reduce the fluorescence intensity but shortens its lifetime as well. Aiming at the quantification of this phenomenon, we turn to temporally resolved measurements.

4. Rapid fluorescence quenching in TMDC hybrids

To be capable of time-resolved detection of even the weak fluorescence from various PO/TMDC hybrids, we performed FLIM on these samples, achieving a higher sensitivity than in the μ-PL spectroscopy and tracking the temporal evolution of the emission signal. For the analysis, spatial and temporal information were regarded separately. First, we take a look at the time-integrated FLIM data for each pixel. Here, in analogy to the μ-PL, the integration yields 2D intensity maps of the scanned sample areas, as illustrated in Fig. 4(a) and (b) for the hBN and WSe_2 flakes shown in Fig. 2(a) and (d), respectively. For hBN, the flake topography is resembled by the intensity of the PO fluorescence varying between different regions of the crystal. Yet, no systematic dependence on the thickness is found and the variation of the overall intensity within the hBN area as well as *versus* the substrate reaches one order of magnitude at most. The PO-coated WSe_2 flakes, in contrast, exhibit an enormous discrepancy compared to the environment, with the intensities dropping by three orders of magnitude. To properly quantify this effect, we determined both the minimum and maximum absolute intensity values for the substrate area and the thinnest flake regions for two different hBN samples as well as for the four 1L-TMDCs. We calculated the minimum relative fluorescence intensity as the ratio of the minimum value on the flake divided by the maximum on the substrate and *vice versa* for the maximum relative intensity. This way, the comparison with the substrate should eliminate differences in dye molecule coverage between the samples. The resulting relative intensity ranges are presented in Fig. 4(c), while the original data for the remaining flakes in terms of 2D maps may be looked up in the ESI, Fig. S9.†

Regarding the relative intensities, we clearly observe a systematic difference between the TMDC monolayers and the hBN references. Surprisingly, the hBN1 and hBN2 samples – albeit prepared in an identical manner – yield clearly different values. However, experiments on a third sample with a slightly higher coverage (hBN3) demonstrated that the fluorescence signal is affected by the formation of PO agglomerates on the hBN surface (see ESI, Section 4.2†). Such agglomerates may form due to diffusion of the molecules on the surface, which

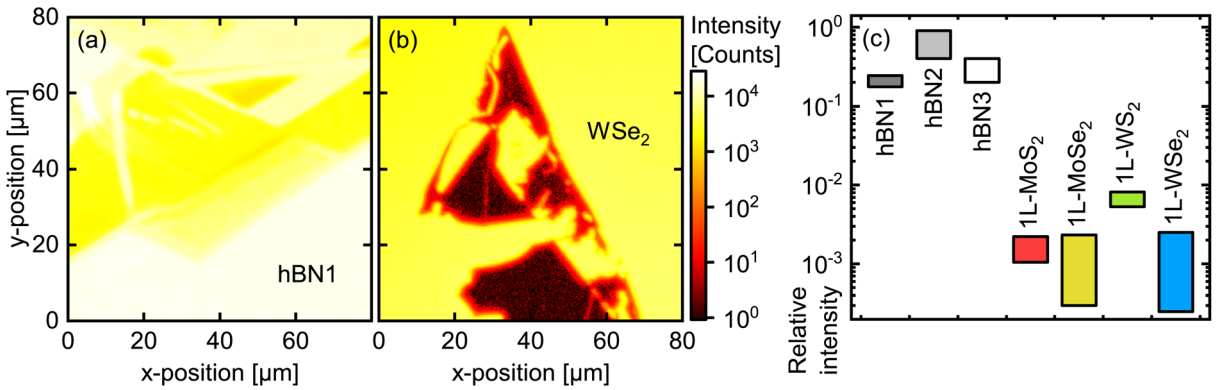

Fig. 4 (a and b) Intensity maps of TVD-coated hBN1 and WSe_2, respectively, as obtained by time-integrating the FLIM data. The depicted areas match the micrographs from Fig. 2(a) and (d), with the crystal topography being clearly reproduced in the FLIM map. The intensity drop from substrate to flake is drastically stronger on WSe_2 than on hBN. (c) FLIM intensity on different 2D flakes relative to their respective substrate environment. The bars cover the uncertainty interval of each value. While the three hBN samples range between 0.2 and near-unity, the 1L-TMDCs exhibit relative intensities in the order of 10^{-3}. As discussed in the ESI, Section 4.2,† the hBN3 sample represents a lower bound for the relative intensity of PO on hBN. Note that the value for WS_2 is overestimated, as there is still some amount of 1L-PL transmitted through the band pass filter (see ESI, Sections 4.3 and 4.4†).

has been monitored by AFM scans (see ESI, Section 3†). As a result, small differences in PO coverage together with varying surface characteristics of the hBN1 and hBN2 flakes can lead to strong distinctions between those samples regarding agglomerate formation and correspondingly differing fluorescence intensities. To exclude this effect, the white bar for hBN3 in Fig. 4(c) represents a largely agglomerate-free region, *i.e.* with a homogeneous, almost pure monomer coating. Considering that the agglomerates form by draining molecules from their environment, this homogeneous area is probably characterized by a lower molecule coverage than the flake in total as well as the surrounding substrate. Consequently, the hBN3 value can be regarded as a lower bound for the relative intensity of the fluorescence of monomer PO on hBN, leaving a range from about 0.3 to unity. The PO/TMDC hybrids, in contrast, reach values of about 10^{-3}, close to the noise level. Merely PO/1L-WS_2 scores 1%. However, in this case, the monolayer PL is strong enough to still contribute some photon counts despite the usage of the band pass filter. Taking this into account, we conclude a fluorescence intensity reduction by a factor of roughly 10^3 on the TMDC monolayers compared to the hBN. This stands out from other hybrid structures with thicker molecular layers where the fluorescence intensity on the 1L-TMDC *vs.* substrate differ by a factor of ten at most.[21,31,32,41] In our case, the planar shape of the molecule probably leads to a face-down orientation on the TMDC monolayers, which in turn promotes efficient charge transfer. Another reason for the drastic effect in our case supposedly lies in the monomeric coating, while in films of several nanometer thickness, excitons have to diffuse towards the interface before charge transfer can take place. This leaves more time for radiative recombination and therefore increases the residual fluorescence intensity. Although these findings strongly point to the occurrence of some quenching mechanism, a final conclusion still requires information on the time evolution of the fluorescence. In order to analyze the emission decay dynamics, we extracted the time-resolved intensity by integrating the FLIM data over the respective regions of interest, namely the substrate, the thinnest hBN areas, and the TMDC monolayers. The obtained normalized time traces are depicted in Fig. 5 as bright, solid lines. For the substrate and the hBN flakes, we observe a fast signal reduction on the sub-nanosecond scale followed by a long-term contribution decaying over several ns. The time traces of the PO/TMDC hybrids, on the contrary, essentially follow the course of the IRF, indicating a decay time constant well below the experimental time resolution.

For a detailed analysis, we fitted the time traces by two exponentials, yielding a good agreement with the data, as can be seen from the dark, dashed lines in Fig. 5. In this process, the signal rise was modeled by an error function. The resulting parameters are summarized in Table 1. For the shorter exponential time constant τ_1 on hBN, we obtain values of a few 100 ps, varying between the different samples and regions. The longer time constant τ_2, in contrast, consistently yields about 3 ns. We assign this to the monomer PO molecules, as it is comparable to the fluorescence lifetime of almost 4 ns in solutions of similar monomers.[56,57] The origin of the shorter

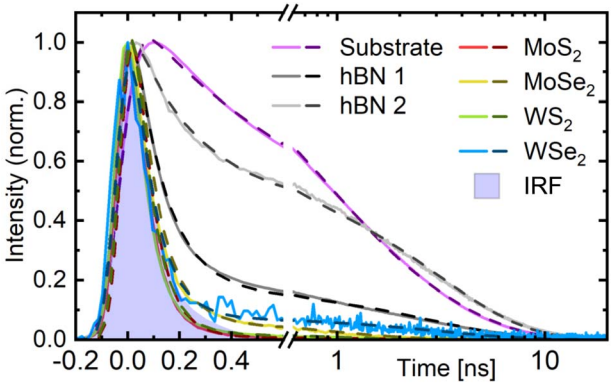

Fig. 5 Normalized fluorescence decay of PO films on different materials. The curves result from integrating the FLIM data over the respective areas of interest. Solid lines represent the data, dashed lines show the fits, which are in good agreement with the data, and the filled area marks the instrument response function. The TMDC curves essentially follow the IRF – despite a small long-living component – while the curves for substrate and hBN show a much slower decrease or at least a long-term tail.

Table 1 Time constants and amplitude ratios from biexponential time trace fitting. All underlying fluorescence time traces were measured employing the 500–550 nm band pass filter. Here, τ_1 for the PO/TMDC hybrids is very close to the time constants for the IRF, indicating that the underlying dynamics could not be separated from the instrument response. The SiO_2 entries represent a summary of the values for the coated wafer environment of all hBN and TMDC samples. The time traces for hBN3 are depicted in the ESI, Fig. S8(b)

Substrate for PO layer	τ_1 [ns]	τ_2 [ns]	$\frac{A_2}{A_1}$
SiO_2	0.5–1.0	2.2–3.2	0.60–1.3
IRF	0.065	0.14	0.53
hBN1	0.12	2.9	0.13
hBN2	0.22	3.1	0.97
hBN3 (homogeneous)	0.46	3.5	3.3
hBN3 (agglomerates)	0.10	2.2	0.045
1L-MoS_2	0.073	1.4	0.0056
1L-$MoSe_2$	0.087	0.92	0.048
1L-WS_2	0.071	0.92	0.015
1L-WSe_2	0.085	3.1	0.050

lifetime can again be elucidated with the help of the hBN3 sample. Here, we were able to separate regions dominated by agglomerates from areas largely governed by homogeneously deposited monomer PO (see ESI Section 4.2†). While for the former regions, the fast decay accounts for most of the amplitude and the slow component almost vanishes, an opposite behavior is observed in the latter. Thus, we conclude that τ_1 can be assigned to energy transfer from excited PO monomers into agglomerate-associated multi-particle states, *e.g.* excimers, which do not emit in the spectral range of the bandpass filter.[20] Furthermore, when comparing the fit parameters for the different hBN flakes and regions, we find

that τ_1 takes smaller values, the higher the amplitude of the fast decay compared to the slow one. This could point to a mechanism where the presence of more or bigger agglomerates actually speeds up the decay, *e.g.* in a diffusion-mediated exciton trapping model. Alternatively, this behavior may result as a fitting artifact from the superposition with the asymmetric IRF. Indeed, the latter can also be fitted biexponentially with $\tau_1 = 65$ ps and $\tau_2 = 140$ ps.

The PO/TMDC hybrids, as already expected from the measured time traces, essentially follow the IRF, manifesting in the values of τ_1 from 70 ps to 90 ps. Note that these only indicate the resolution limit as determined by the IRF. They are not to be confused with the actual time constants of the underlying physical processes, which lie well below the time resolution of this setup. In addition to the fast decay, the fits reveal different, yet in any case weak long-term contributions to the time traces. Following the interpretation of charge or energy transfer-induced quenching, this tail could stem from imperfect contact between the dye and the TMDC layer, leaving some PO molecules only weakly or even unquenched. They would emit residual long-living fluorescence, thereby leading to an overestimation of the relative intensity on the PO/TMDC hybrid structures in Fig. 4(c) as well.

With this information and taking into account the intensity ratios discussed above, we can estimate the time constant of the nonradiative decay. For hBN, the relative intensity takes values of 0.3–1, although in the case of the hBN2 sample with a prevailing monomer contribution in the decay, it approaches unity. In contrast, the TMDCs achieve values of about 10^{-3}. Assuming a comparable PO coverage due to the similar surface, we obtain a quenching factor of nearly 10^3. As this also resembles the ratio of the nonradiative *vs.* the radiative time constant of 3 ns, we end up with a charge or energy transfer time from dye to semiconductor of several picoseconds. Yet, we have to consider that even the hBN2 area shows agglomerate features in the time trace. This results in a lower fluorescence than for a perfect monomer coating and thus an underestimation of the quenching in the PO/TMDC hybrids. The same holds for the possibly imperfect contact of the molecules on the respective 2D material that – in the case of the TMDCs – would inhibit charge or energy transfer for a fraction of the molecules and thus reduce the observed quenching. All taken together, this is in agreement with charge transfer time constants of 40 up to several 100 fs for metal phtalocyanine/TMDC hybrid systems.[29–32]

5. Conclusion

In this study, we investigated PO/1L-TMDC hybrid structures with a molecular sub-monolayer by means of μ-PL spectroscopy and FLIM to gather evidence for charge or energy transfer after optical excitation. We observe a drastic reduction of the dye fluorescence intensity on all TMDCs, as opposed to the PO/hBN references. Simultaneously, the lifetime of the emission signal is strongly reduced from about 3 ns to values well below the FLIM time resolution. This verifies the occurrence of a strong quenching mechanism induced by the TMDC monolayers. *Vice versa*, the deposition of PO molecules enhances the trion emission of WSe_2 at low temperatures. This cannot be accounted for by charge transfer, so it may result from the PO screening defects of the monolayer. Based on the quenching ratio and the radiative lifetime of the unquenched dye monomers, we deduced an upper limit for the corresponding hole or energy transfer time constant in the order of several picoseconds. These results are in line with previous research on charge transfer in metal phtalocyanines and pave the way for its exploitation in optoelectronic devices.

Author contributions

T. V., S. L., T. K., I. B., and S. S. conceptualized and planned the project as well as contributed to writing the manuscript. T. V., A. S. and E. O. tested and established the coating techniques. K. W. and T. T. provided the hBN bulk crystals. R. S. set up the μ-PL spectroscopy. T. V. and A. S. performed the preparation and optical characterization of the hybrid structures at room temperature. T. V. and J. S. executed the low-temperature experiments. I. B. conducted the AFM measurements. S. L., T. K., and S. S. supervised the project.

Conflicts of interest

There are no conflicts to declare.

Acknowledgements

This work was funded by the Deutsche Forschungsgemeinschaft (DFG, German Research Foundation) – SFB 1477 "Light–Matter Interactions at Interfaces", project number 441234705. T. V. expresses his gratitude to the University of Rostock for its financial support *via* the PhD Scholarship Program. T. K. gratefully acknowledges funding by the DFG *via* grant no. KO 3612/7-1, project number 467549803. K. W. and T. T. acknowledge support from the JSPS KAKENHI (grant numbers 20H00354 and 23H02052). We thank Regina Lange for assisting the AFM measurements.

References

1 K. F. Mak, C. Lee, J. Hone, J. Shan and T. F. Heinz, *Phys. Rev. Lett.*, 2010, **105**, 136805.
2 A. Splendiani, L. Sun, Y. Zhang, T. Li, J. Kim, C.-Y. Chim, G. Galli and F. Wang, *Nano Lett.*, 2010, **10**, 1271–1275.
3 T. Cheiwchanchamnangij and W. R. L. Lambrecht, *Phys. Rev. B: Condens. Matter Mater. Phys.*, 2012, **85**, 205302.
4 T. Völzer, F. Fennel, T. Korn and S. Lochbrunner, *Phys. Rev. B*, 2021, **103**, 045423.
5 M. Kulig, J. Zipfel, P. Nagler, S. Blanter, C. Schüller, T. Korn, N. Paradiso, M. M. Glazov and A. Chernikov, *Phys. Rev. Lett.*, 2018, **120**, 207401.
6 K. F. Mak and J. Shan, *Nat. Photonics*, 2016, **10**, 216–226.
7 M. M. Furchi, A. Pospischil, F. Libisch, J. Burgdörfer and T. Mueller, *Nano Lett.*, 2014, **14**, 4785–4791.

8 D. Somvanshi and S. Jit, *2D Nanoscale Heterostructured Materials*, Elsevier, 2020, pp. 125–149.
9 N. Ubrig, E. Ponomarev, J. Zultak, D. Domaretskiy, V. Zólyomi, D. Terry, J. Howarth, I. Gutiérrez-Lezama, A. Zhukov, Z. R. Kudrynskyi, Z. D. Kovalyuk, A. Patané, T. Taniguchi, K. Watanabe, R. V. Gorbachev, V. I. Fal'ko and A. F. Morpurgo, *Nat. Mater.*, 2020, **19**, 299–304.
10 M. Massicotte, P. Schmidt, F. Vialla, K. G. Schädler, A. Reserbat-Plantey, K. Watanabe, T. Taniguchi, K. J. Tielrooij and F. H. L. Koppens, *Nat. Nanotechnol.*, 2015, **11**, 42–46.
11 D. Jariwala, T. J. Marks and M. C. Hersam, *Nat. Mater.*, 2016, **16**, 170–181.
12 S. Padgaonkar, J. N. Olding, L. J. Lauhon, M. C. Hersam and E. A. Weiss, *Acc. Chem. Res.*, 2020, **53**, 763–772.
13 X. Hong, J. Kim, S.-F. Shi, Y. Zhang, C. Jin, Y. Sun, S. Tongay, J. Wu, Y. Zhang and F. Wang, *Nat. Nanotechnol.*, 2014, **9**, 682–686.
14 C. Jin, E. Y. Ma, O. Karni, E. C. Regan, F. Wang and T. F. Heinz, *Nat. Nanotechnol.*, 2018, **13**, 994–1003.
15 F. Fennel and S. Lochbrunner, *Phys. Rev. B: Condens. Matter Mater. Phys.*, 2012, **85**, 094203.
16 T. Förster, *Ann. Phys.*, 1948, **437**, 55–75.
17 Z. Cai, B. Liu, X. Zou and H.-M. Cheng, *Chem. Rev.*, 2018, **118**, 6091–6133.
18 S. Shree, A. George, T. Lehnert, C. Neumann, M. Benelajla, C. Robert, X. Marie, K. Watanabe, T. Taniguchi, U. Kaiser, B. Urbaszek and A. Turchanin, *2D Mater.*, 2019, **7**, 015011.
19 F. Würthner, C. R. Saha-Möller, B. Fimmel, S. Ogi, P. Leowanawat and D. Schmidt, *Chem. Rev.*, 2015, **116**, 962–1052.
20 A. L. Bialas and F. C. Spano, *J. Phys. Chem. C*, 2022, **126**, 4067–4081.
21 I. K. Sideri, Y. Jang, J. Garcés-Garcés, Á. Sastre-Santos, R. Canton-Vitoria, R. Kitaura, F. Fernández-Lázaro, F. D'Souza and N. Tagmatarchis, *Angew. Chem., Int. Ed.*, 2021, **60**, 9120–9126.
22 S. Roy, A. S. Sharbirin, Y. Lee, W. B. Kim, T. S. Kim, K. Cho, K. Kang, H. S. Jung and J. Kim, *Nanomaterials*, 2020, **10**, 1032.
23 J. Choi, H. Zhang and J. H. Choi, *ACS Nano*, 2016, **10**, 1671–1680.
24 H. Nan, Z. Wang, W. Wang, Z. Liang, Y. Lu, Q. Chen, D. He, P. Tan, F. Miao, X. Wang, J. Wang and Z. Ni, *ACS Nano*, 2014, **8**, 5738–5745.
25 S. Mouri, Y. Miyauchi and K. Matsuda, *Nano Lett.*, 2013, **13**, 5944–5948.
26 S. Park, T. Schultz, X. Xu, B. Wegner, A. Aljarb, A. Han, L.-J. Li, V. C. Tung, P. Amsalem and N. Koch, *Commun. Phys.*, 2019, **2**, 109.
27 S. B. Homan, V. K. Sangwan, I. Balla, H. Bergeron, E. A. Weiss and M. C. Hersam, *Nano Lett.*, 2016, **17**, 164–169.
28 T. Zhu, L. Yuan, Y. Zhao, M. Zhou, Y. Wan, J. Mei and L. Huang, *Sci. Adv.*, 2018, **4**, eaao3104.
29 C. Zhong, V. K. Sangwan, C. Wang, H. Bergeron, M. C. Hersam and E. A. Weiss, *J. Phys. Chem. Lett.*, 2018, **9**, 2484–2491.
30 S. Padgaonkar, S. H. Amsterdam, H. Bergeron, K. Su, T. J. Marks, M. C. Hersam and E. A. Weiss, *J. Phys. Chem. C*, 2019, **123**, 13337–13343.
31 T. R. Kafle, B. Kattel, S. D. Lane, T. Wang, H. Zhao and W.-L. Chan, *ACS Nano*, 2017, **11**, 10184–10192.
32 T. R. Kafle, B. Kattel, P. Yao, P. Zereshki, H. Zhao and W.-L. Chan, *J. Am. Chem. Soc.*, 2019, **141**, 11328–11336.
33 Y. Kong, S. M. Obaidulla, M. R. Habib, Z. Wang, R. Wang, Y. Khan, H. Zhu, M. Xu and D. Yang, *Mater. Horiz.*, 2022, **9**, 1253–1263.
34 T. Scharl, G. Binder, X. Chen, T. Yokosawa, A. Cadranel, K. C. Knirsch, E. Spiecker, A. Hirsch and D. M. Guldi, *J. Am. Chem. Soc.*, 2022, **144**, 5834–5840.
35 C. Ramanan, A. L. Smeigh, J. E. Anthony, T. J. Marks and M. R. Wasielewski, *J. Am. Chem. Soc.*, 2011, **134**, 386–397.
36 D. Wickramaratne, L. Weston and C. G. V. de Walle, *J. Phys. Chem. C*, 2018, **122**, 25524–25529.
37 Z. Cao, M. Harb, S. Lardhi and L. Cavallo, *J. Phys. Chem. Lett.*, 2017, **8**, 1664–1669.
38 J. Kang, S. Tongay, J. Zhou, J. Li and J. Wu, *Appl. Phys. Lett.*, 2013, **102**, 012111.
39 C. Gong, H. Zhang, W. Wang, L. Colombo, R. M. Wallace and K. Cho, *Appl. Phys. Lett.*, 2013, **103**, 053513.
40 V. Iberi, L. Liang, A. V. Ievlev, M. G. Stanford, M.-W. Lin, X. Li, M. Mahjouri-Samani, S. Jesse, B. G. Sumpter, S. V. Kalinin, D. C. Joy, K. Xiao, A. Belianinov and O. S. Ovchinnikova, *Sci. Rep.*, 2016, **6**, 30481.
41 X. Liu, J. Gu, K. Ding, D. Fan, X. Hu, Y.-W. Tseng, Y.-H. Lee, V. Menon and S. R. Forrest, *Nano Lett.*, 2017, **17**, 3176–3181.
42 A. Castellanos-Gomez, M. Buscema, R. Molenaar, V. Singh, L. Janssen, H. S. J. van der Zant and G. A. Steele, *2D Mater.*, 2014, **1**, 011002.
43 J. Lub, P. A. van Hal, R. Smits, L. Malassenet, J. Pikkemaat and R. A. Hikmet, *J. Lumin.*, 2019, **207**, 585–588.
44 L. Renn, L. S. Walter, K. Watanabe, T. Taniguchi and R. T. Weitz, *Adv. Mater. Interfaces*, 2022, **9**, 2101701.
45 K. F. Mak, K. He, C. Lee, G. H. Lee, J. Hone, T. F. Heinz and J. Shan, *Nat. Mater.*, 2012, **12**, 207–211.
46 J. Jadczak, M. Glazov, J. Kutrowska-Girzycka, J. J. Schindler, J. Debus, C.-H. Ho, K. Watanabe, T. Taniguchi, M. Bayer and L. Bryja, *ACS Nano*, 2021, **15**, 19165–19174.
47 D. Kiriya and D.-H. Lien, *Nano Express*, 2022, **3**, 034002.
48 G. Wang, E. Palleau, T. Amand, S. Tongay, X. Marie and B. Urbaszek, *Appl. Phys. Lett.*, 2015, **106**, 112101.
49 P. Nagler, M. V. Ballottin, A. A. Mitioglu, M. V. Durnev, T. Taniguchi, K. Watanabe, A. Chernikov, C. Schüller, M. M. Glazov, P. C. Christianen and T. Korn, *Phys. Rev. Lett.*, 2018, **121**, 057402.
50 F. S. Conrad-Burton, T. Liu, F. Geyer, R. Costantini, A. P. Schlaus, M. S. Spencer, J. Wang, R. H. Sánchez, B. Zhang, Q. Xu, M. L. Steigerwald, S. Xiao, H. Li, C. P. Nuckolls and X. Zhu, *J. Am. Chem. Soc.*, 2019, **141**, 13143–13147.
51 Z. Yu, Y. Wu, Q. Peng, C. Sun, J. Chen, J. Yao and H. Fu, *Chem.–Eur. J.*, 2016, **22**, 4717–4722.
52 T. Godde, D. Schmidt, J. Schmutzler, M. Aßmann, J. Debus, F. Withers, E. M. Alexeev, O. D. Pozo-Zamudio, O. V. Skrypka,

K. S. Novoselov, M. Bayer and A. I. Tartakovskii, *Phys. Rev. B*, 2016, **94**, 165301.

53 Z. Li, T. Wang, Z. Lu, C. Jin, Y. Chen, Y. Meng, Z. Lian, T. Taniguchi, K. Watanabe, S. Zhang, D. Smirnov and S.-F. Shi, *Nat. Commun.*, 2018, **9**, 3719.

54 J. J. P. Thompson, V. Lumsargis, M. Feierabend, Q. Zhao, K. Wang, L. Dou, L. Huang and E. Malic, *Nanoscale*, 2023, **15**, 1730–1738.

55 L. Zhang, F. Zhou, X. Zhang, S. Yang, B. Wen, H. Yan, T. Yildirim, X. Song, Q. Yang, M. Tian, N. Wan, H. Song, J. Pei, S. Qin, J. Zhu, S. Wageh, O. A. Al-Hartomy, A. G. Al-Sehemi, H. Shen, Y. Liu and H. Zhang, *Adv. Mater.*, 2022, 2206212.

56 F. Würthner, *Chem. Commun.*, 2004, 1564–1579.

57 W. E. Ford and P. V. Kamat, *J. Phys. Chem.*, 1987, **91**, 6373–6380.